

1 **Equilibrium climate sensitivity increases with aerosol concentration**  
2 **due to changes in precipitation efficiency**

3 Guy Dagan<sup>1\*</sup>

4 <sup>1</sup> Fredy and Nadine Herrmann Institute of Earth Sciences, Hebrew University,  
5 Jerusalem, Israel

6 \*Corresponding author. Email: [guy.dagan@mail.huji.ac.il](mailto:guy.dagan@mail.huji.ac.il)

7

8

9

10

11

12

13

14

15

16

17

18

19

20

21

22

23

24

25

26

27

28

29

30

31

32

33

## 34 **Abstract**

35 How Earth's climate reacts to anthropogenic forcing is one of the most burning  
36 questions faced by today's scientific community. A leading source of uncertainty in  
37 estimating this sensitivity is related to the response of clouds. Under the canonical  
38 climate-change perspective of forcings and feedbacks, the effect of anthropogenic  
39 aerosols on clouds is categorized under the forcing component, while the modifications  
40 of the radiative properties of clouds due to climate change are considered in the  
41 feedback component. Each of these components contributes the largest portion of  
42 uncertainty to its relevant category and is largely studied separately from the other. In  
43 this paper, using idealized cloud resolving, radiative-convective-equilibrium  
44 simulations, with a slab ocean model, we show that aerosol-cloud interactions could  
45 affect cloud feedback. Specifically, we show that equilibrium climate sensitivity  
46 increases under high aerosol concentration due to an increase in the shortwave cloud  
47 feedback. The shortwave cloud feedback is enhanced under high aerosol conditions due  
48 to a stronger increase in the precipitation efficiency with warming, which can be  
49 explained by higher sensitivity of the droplet size and the cloud water content to the  
50 CO<sub>2</sub> concentration rise. These results indicate a possible connection between cloud  
51 feedback and aerosol-cloud interactions.

52

## 53 **1. Introduction**

54 Estimating Earth's equilibrium climate sensitivity (ECS), defined as the steady-state  
55 global mean temperature increase for a doubling of CO<sub>2</sub>, is considered as a first-order,  
56 fundamental milestone on the way to understanding and predicting anthropogenic-  
57 driven climate change (Sherwood et al., 2020). Decades of research have tried to  
58 accurately quantify ECS, with only limited success. The most probable current ECS  
59 estimates are in the range of 2.3–4.5K (Sherwood et al., 2020). The largest source of  
60 uncertainty in estimating ECS is related to the response of clouds to the externally  
61 forced warming and the feedback of these changes on the climate system (Sherwood et  
62 al., 2020; Ceppi et al., 2017; Schneider et al., 2017). Clouds strongly modulate Earth's  
63 radiation budget by reflecting the incoming shortwave radiation from the sun and by  
64 absorbing and re-emitting the terrestrial longwave radiation (Loeb et al., 2018). Thus,  
65 changes in the cloud macro-physical properties (such as coverage and vertical extent)  
66 and micro-physical properties (such as liquid/ice partition or hydrometeors size) due to  
67 anthropogenic-driven climate change could significantly alter the climate system's

68 response (Gettelman and Sherwood, 2016; Nuijens and Siebesma, 2019; Schneider et  
69 al., 2017).

70 An important factor in determining cloud feedback magnitude is the sensitivity of the  
71 Precipitation Efficiency ( $\epsilon$ ) (Lutsko et al., 2021; Li et al., 2022; Lutsko and Cronin,  
72 2018).  $\epsilon$  quantifies the fraction of condensed water in a cloud to reach the surface as  
73 precipitation. Using idealized cloud resolving simulations, it was shown that  $\epsilon$  is  
74 expected to increase with temperature (Lutsko and Cronin, 2018). The increase in  $\epsilon$   
75 with warming was shown to be mostly driven by an increase in the efficiency with  
76 which cloud condensate is converted into precipitation, while changes in the  
77 evaporation of falling precipitation was shown to play a smaller role (Lutsko and  
78 Cronin, 2018).

79 An increase in  $\epsilon$  with warming represents more efficient depletion of the water from  
80 the clouds, thus affecting the radiation budget. On the one hand, increase in  $\epsilon$  with  
81 warming was suggested to reduce the anvil cloud coverage and hence increase the  
82 outgoing longwave radiation (Lindzen et al., 2001; Mauritsen and Stevens, 2015), thus  
83 producing negative feedback. On the other hand, however, it was recently shown that  
84 the longwave effect of an  $\epsilon$  increase is over-compensated for by changes in the  
85 shortwave flux (Li et al., 2019), i.e., a large reduction in the cloud optical depth, driving  
86 a reduction in the shortwave cooling effect of clouds, dominates the response.

87 The efficiency with which cloud condensate is converted into precipitation is closely  
88 linked to the micro-physical properties of the clouds. The autoconversion of cloud  
89 droplets into rain becomes significant when liquid water amount and/or droplet radii  
90 reach a critical threshold (Freud and Rosenfeld, 2012). An important factor influencing  
91 the droplet radii (and also the liquid water amount, to some degree) is the amount of  
92 available cloud condensation nuclei (CCN). Generally, an increase in aerosol  
93 concentration drives an increase in CCN concentration, which results in more numerous  
94 and smaller droplets in the cloud (Twomey, 1974; Warner and Twomey, 1967). The  
95 smaller droplets require longer time (or equivalently larger vertical distance) in the  
96 clouds to grow by diffusion to the critical size enabling precipitation, thus delaying the  
97 initial warm rain formation (Rosenfeld, 2000; Dagan et al., 2015b). In addition, aerosols  
98 were suggested to enhance the vertical velocities and the cloud top heights of deep  
99 convective clouds (due to the so-called invigoration mechanism (Abbott & Cronin,  
100 2021; Koren et al., 2005; Rosenfeld et al., 2008)), which in turn can results in

101 precipitation enhancement (Koren et al., 2012). Therefore, aerosols could affect  $\epsilon$   
102 (Khain, 2009).

103 In addition to the effect on rain, aerosols could modify the radiative properties of clouds,  
104 by modifying the droplet concentration and size distribution (Twomey, 1974) and by  
105 affecting the clouds' macro-physical properties (Albrecht, 1989; Bellouin et al., 2019).  
106 These changes to the radiative properties of clouds result in radiative forcing that could  
107 affect the sea surface temperature [SST (Bellouin et al., 2019)]. Using cloud-resolving  
108 radiative-convective-equilibrium simulations with interactive SST, Khairoutdinov and  
109 Yang (2013) showed that the surface temperature decreases by 1.5K with each 10-fold  
110 increase in aerosol concentration, an effect quite comparable to a 2.1–2.3K SST  
111 warming obtained in a simulation with given (low) aerosol conditions but doubled CO<sub>2</sub>  
112 concentration.

113 It has been suggested that cloud feedback and aerosol forcing are not independent of  
114 each other (Mülmenstädt and Feingold, 2018; Igel and van den Heever, 2021). In  
115 addition, the strong links between  $\epsilon$  and cloud feedback and between  $\epsilon$  and aerosol  
116 concentration merit a dedicated study on the potential mutual CO<sub>2</sub> and aerosol effect on  
117 clouds and thus also on ECS, which is the aim of the current study.

118  
119

## 120 2. Methods

### 121 Model description and experimental design

122 The model used herein is the System of Atmospheric Modeling [SAM - (Khairoutdinov  
123 and Randall, 2003)] version 6.11.7. Subgrid-scale fluxes are parameterized using  
124 Smagorinsky's eddy diffusivity model and gravity waves are damped at the top of the  
125 domain. The microphysics scheme used is Morrison et al. (2005) 2-moment bulk  
126 microphysics. The cloud droplet number concentration source assumes that the number  
127 of activated CCN depends on the super-saturation ( $S$  – which is estimated diagnostically  
128 in the model as the model assumes saturation adjustment) according to a power-law:  
129  $CDNC = N_a S^k$ , where  $N_a$  is the prescribed concentration of CCN active at 1 % super-  
130 saturation, and  $k$  is a constant (set in this study to 0.4 - a typical value for maritime  
131 conditions). Changes in  $N_a$  serve as a proxy for the change in aerosol concentration.  
132 Three levels of  $N_a$  are considered here, covering an extreme range of conditions – 20,  
133 200 and 2000 cm<sup>-3</sup>. While this wide range of conditions is unlikely to exist at any given

134 geographical location, they are used here in order to cover the range of possible  
135 conditions at different locations and to maximize the effect for establishing better  
136 physical understanding. The activation of CCN at the cloud base is parameterized  
137 following Twomey (1959), using the vertical velocity and CCN spectrum parameters.  
138 The model is configured to pass cloud water and ice-crystal effective radii from the  
139 microphysics scheme to the radiation scheme; thus, the Twomey effect (Twomey,  
140 1977) of both liquid and ice is considered. Direct interactions between aerosols and  
141 radiation are not considered here.

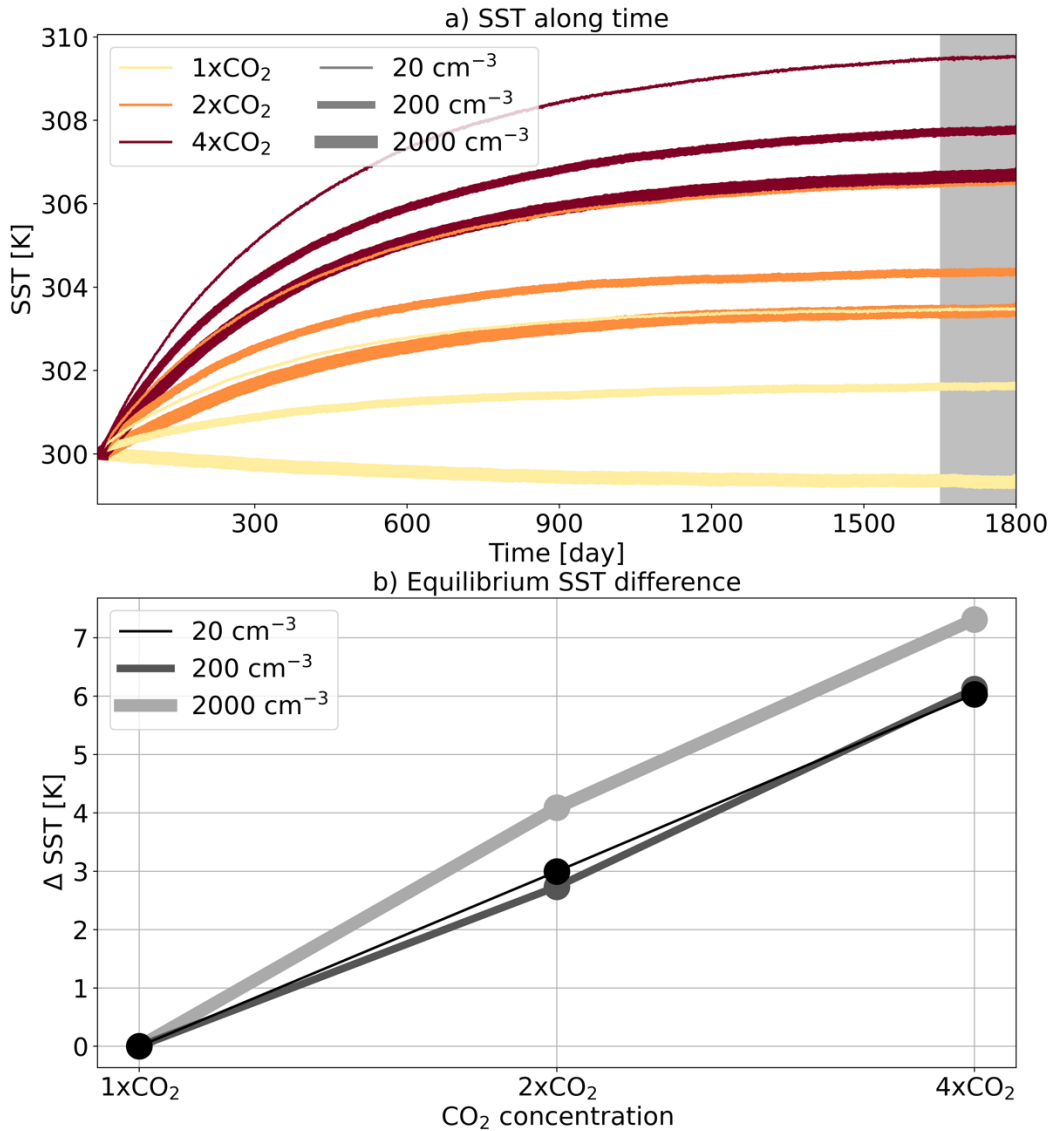
142 The simulations are conducted in a radiative-convective-equilibrium (RCE) mode and  
143 generally follow the RCEMIP (RCE model inter-comparison project (Wing et al.,  
144 2018)) small-domain instructions (but with interactive SST and changes in the CO<sub>2</sub> and  
145 aerosol concentration). The simulations were performed on a square, doubly periodic  
146 domain. In this case, we want to avoid the effect of convective self-aggregation on  $\epsilon$ ;  
147 thus, the domain size is set to 96x96 km<sup>2</sup>, which was shown to be small enough to  
148 prevent convective self-aggregation (Muller and Held, 2012; Lutsko and Cronin, 2018;  
149 Yanase et al., 2020). The horizontal grid spacing is set to 1km and 68 vertical levels are  
150 used, between 25m and 31km, with vertical grid spacing increasing from 50m near the  
151 surface to roughly 1km at the domain top. We note that while shallow clouds are present  
152 in the simulations, the grid spacing used here is too coarse for a full representation of  
153 these clouds. A time step of 10s is used, and radiative fluxes are calculated every 5 min  
154 using the CAM radiation scheme (Collins et al., 2006). The output resolution for all  
155 fields is 1h (3D fields are saved as snapshots while domain statistics are saved as  
156 hourly-averages). The incoming solar radiation is fixed at 551.58 Wm<sup>-2</sup> with a zenith  
157 angle of 42.05° (Wing et al., 2018), producing a net insolation close to the tropical-  
158 mean value. Convection is initialized with a small thermal noise added near the surface  
159 at the beginning of the simulation. The initial conditions for the simulations are as in  
160 Wing et al. (2018).

161 Greenhouse gases are varied for three different levels: pre-industrial level (280 PPM,  
162 1xCO<sub>2</sub>), 2 times pre-industrial level (2xCO<sub>2</sub>) and 4 times pre-industrial level (4xCO<sub>2</sub>).  
163 As in the case of the aerosol concentrations, the large range of CO<sub>2</sub> conditions covered  
164 here are used to examine the clouds' sensitivity to greenhouse gas concentrations under  
165 a wide range of conditions. Nine different simulations, with all possible combinations  
166 of  $N_a$  and CO<sub>2</sub> concentrations, were conducted. The O<sub>3</sub> vertical profile is similar to

167 Wing et al. (2018) and represents a typical tropical atmosphere. The effect of other trace  
168 gases (such as CH<sub>4</sub> and N<sub>2</sub>O) is neglected for simplicity.

169 In all simulations, the SST is interactive and predicted by a slab ocean model (SOM).  
170 The SOM's mixed layer depth is set to 5m, which represented a compromise between a  
171 relatively deep layer ( $\geq 10\text{m}$ ), which reduces SST noise (Khairoutdinov and Yang,  
172 2013), and a relatively shallow layer ( $\ll 1\text{m}$ ), which requires a shorter computation time  
173 for equilibrium (Romps, 2020). As in Romps (2020), the SOM is cooled at a rate of  $112$   
174  $\text{Wm}^{-2}$  in order to ensure that the simulations with  $1\text{xCO}_2$  are kept at around the initial  
175 SST of  $300\text{K}$  (Fig. 1). Each simulation was run for 1800 days, which is sufficient for  
176 reaching close to equilibrium (the surface energy imbalance is  $\leq 0.1\text{Wm}^{-2}$  in all  
177 simulations during the last 150 days). The last 150 days of each run are used for  
178 statistical sampling (gray shading in Fig. 1).

179



180

181 **Figure 1. a) the sea surface temperature (SST) along time for the different simulations**  
 182 **conducted under different aerosol and CO<sub>2</sub> concentrations. The gray shaded area is**  
 183 **referred to as equilibrium conditions. b) Change in equilibrium SST due to a change in**  
 184 **CO<sub>2</sub> concentration (compared to the 1xCO<sub>2</sub> case of each aerosol concentration), for the**  
 185 **different aerosol concentrations (the different curves).**

186

187

### 188 3. Results

189 Figure 1 presents the SST of the different simulations along time (panel a) and the  
 190 change in the equilibrium SST with the CO<sub>2</sub> concentration for the different  $N_a$  cases  
 191 (panel b). As expected, the equilibrium SST (gray shading in Fig. 1a) increases with the  
 192 CO<sub>2</sub> concentration and decreases with  $N_a$  concentration. However, the rate of increase

193 in equilibrium SST with CO<sub>2</sub> concentration increases under extremely high  $N_a$   
 194 concentrations (2000 cm<sup>-3</sup>), compared with the low and medium  $N_a$  concentrations (20  
 195 and 200 cm<sup>-3</sup>, respectively - Fig. 1b). Calculating the average ECS based on the three  
 196 combinations available for each  $N_a$  condition [2xCO<sub>2</sub>-1xCO<sub>2</sub>, 4xCO<sub>2</sub>-2xCO<sub>2</sub> and  
 197 (4xCO<sub>2</sub>-1xCO<sub>2</sub>)/2], demonstrates that it increases with  $N_a$  from 3.0K at the lowest  $N_a$   
 198 to 3.7K at the highest  $N_a$  (i.e., a 23% increase – Table 1).

199

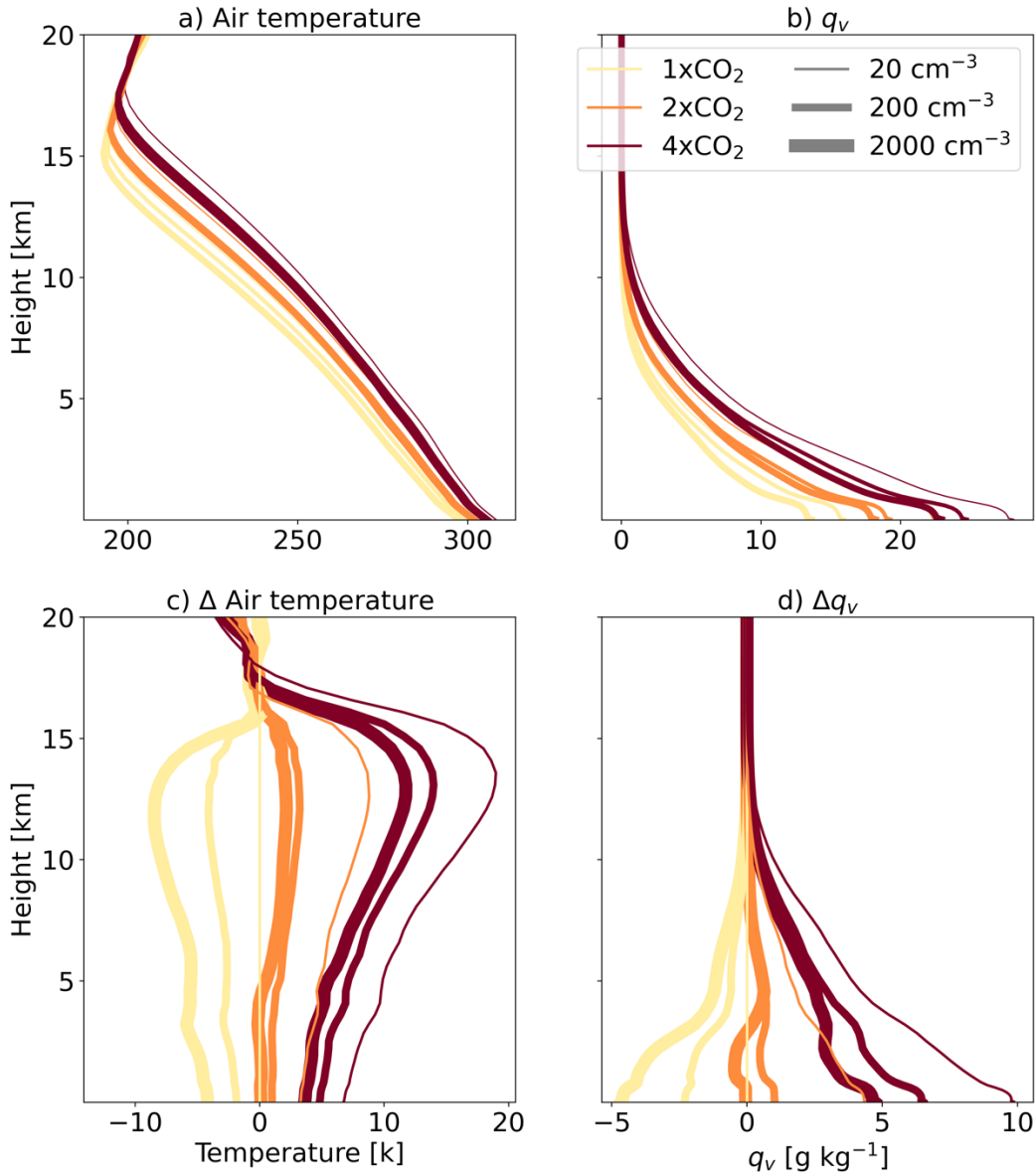
200 **Table 1. Average equilibrium climate sensitivity (ECS), cloud-feedback parameter ( $\lambda_{\text{cloud}}$ ),**  
 201 **hydrological sensitivity ( $\eta$ ), and change in precipitation efficiency ( $\Delta\epsilon$ ) of the three**  
 202 **combinations available for each  $N_a$  condition [2xCO<sub>2</sub>-1xCO<sub>2</sub>, 4xCO<sub>2</sub>-2xCO<sub>2</sub> and 4xCO<sub>2</sub>-**  
 203 **1xCO<sub>2</sub>]. For the calculation of the average ECS, the difference between 4xCO<sub>2</sub> and 1xCO<sub>2</sub>**  
 204 **is divided by 2. The rest of the quantities are normalized by the SST change between the**  
 205 **relevant simulations. Please refer to the text for the definitions of these quantities.**

$N_a$ [cm <sup>-3</sup> ]	ECS [K]	$\lambda_{\text{cloud}}$ [W m <sup>-2</sup> K <sup>-1</sup> ]	$\eta$ [% K <sup>-1</sup> ]	$\Delta\epsilon$ [% K <sup>-1</sup> ]
20	3.0	-0.45	3.8	1.2
200	3.1	-0.38	4.3	1.3
2000	3.7	-0.08	4.6	2.7

206

207 Figure 2 presents the time and domain mean vertical profiles of temperature and water  
 208 vapor mixing ratio ( $q_v$ ) in the different simulations (panels a and b) and their difference  
 209 from the simulation with the lowest  $N_a$  and CO<sub>2</sub> concentrations (panels c and d). It  
 210 demonstrates, as expected, that the vertical profile of air temperature is set by the  
 211 surface temperature (increases with CO<sub>2</sub> concentrations and decreases with  $N_a$ ) with an  
 212 amplification of the change at the upper troposphere, as the profiles follow the moist  
 213 adiabatic lapse-rate. It also shows that  $q_v$  increases with the temperature, as expected  
 214 (Held and Soden, 2006).

215



216

217 **Figure 2. Time and domain mean vertical profiles of air temperature and water vapor**  
 218 **mixing ratio ( $q_v$ ) in the different simulations (a and b) and how they differ from the**  
 219 **simulation with the lowest  $N_a$  and CO<sub>2</sub> concentrations (panels c and d).**

220

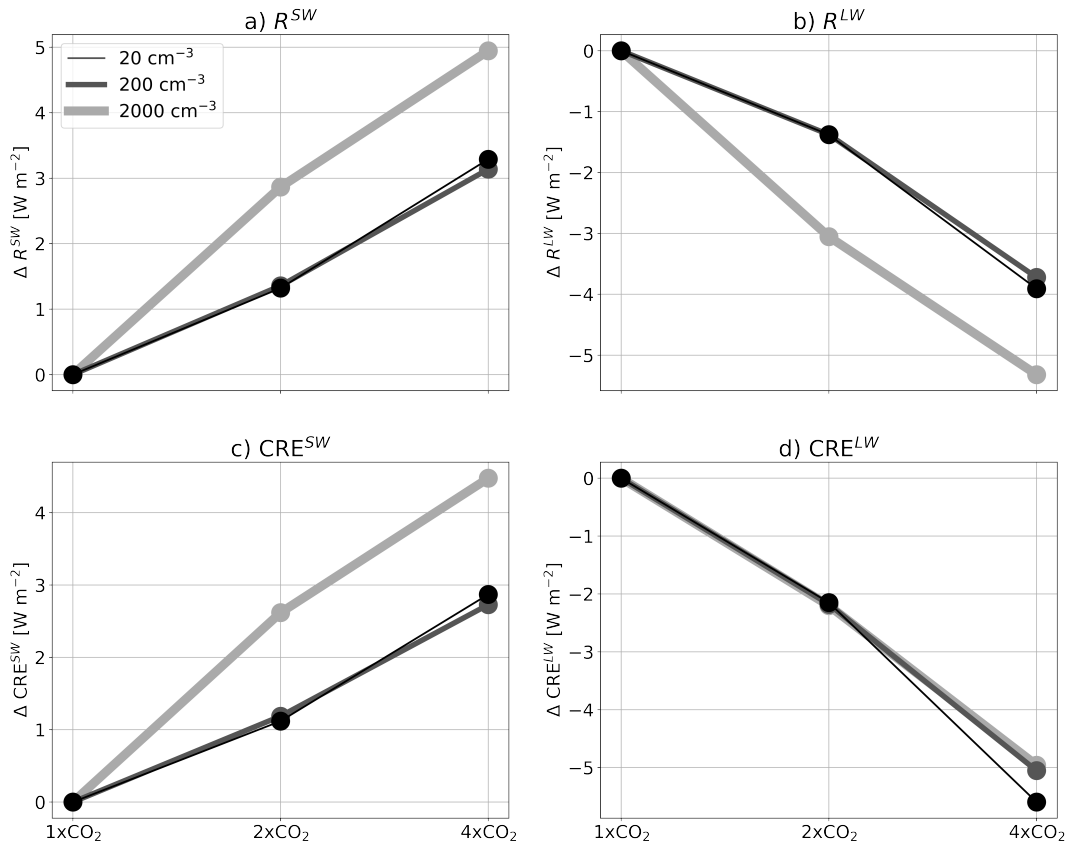
221

222 In order to understand the increase in ECS with  $N_a$ , we next examine the top-of-  
 223 atmosphere (TOA) energy budget. Figure 3 presents the change in the net shortwave  
 224 and longwave TOA energy gain ( $R^{SW}$  and  $R^{LW}$ , respectively) with the CO<sub>2</sub>  
 225 concentration for the different  $N_a$  conditions. In addition, Fig. 3 presents the change in  
 226 the cloud radiative effect (CRE) with increasing the CO<sub>2</sub> concentration, where CRE is  
 227 computed by subtracting the clear-sky from the all-sky TOA radiative fluxes

228  $(R - R_{\text{clear-sky}})$ , again for the shortwave and longwave separately ( $\text{CRE}^{\text{SW}}$  and  $\text{CRE}^{\text{LW}}$ ,  
229 respectively). Figure 3a and b demonstrates that under equilibrium conditions  $R^{\text{SW}}$   
230 increases, while  $R^{\text{LW}}$  decreases with the  $\text{CO}_2$  concentration. However, the rate of change  
231 in both  $R^{\text{SW}}$  and  $R^{\text{LW}}$  is much faster under the high  $N_a$  conditions than under the low  
232 and medium  $N_a$  conditions. The trend in  $\text{CRE}^{\text{SW}}$  under the different  $N_a$  conditions (Fig.  
233 3c) resembles the trend in  $R^{\text{SW}}$ , suggesting that the clouds' response dominates the  
234 changes in the TOA shortwave fluxes.  $\text{CRE}^{\text{LW}}$ , on the other hand, decreases at a similar  
235 rate with  $\text{CO}_2$  concentration for the different  $N_a$  conditions (Fig. 3d). Thus, the different  
236 decrease rates in  $R^{\text{LW}}$  with  $\text{CO}_2$  concentration for the different  $N_a$  conditions (Fig. 3b)  
237 must be driven by clear-sky changes (specifically, the plank, the lapse-rate and the  
238 water vapor feedbacks – see Fig. 2 above).

239 In Table 1 above, we estimate the average cloud radiative feedback ( $\lambda_{\text{cloud}}$ ) as the change  
240 in CRE with increasing surface temperature, i.e.,  $\lambda_{\text{cloud}} = d\text{CRE}/dT$ , for the different  $N_a$   
241 conditions. The table shows that  $\lambda_{\text{cloud}}$  becomes less negative with the increase in  $N_a$ ,  
242 leading to higher climate sensitivity. The differences in the values of  $\lambda_{\text{cloud}}$  between the  
243 different  $N_a$  conditions is mostly derived from the shortwave part of the spectrum (Fig.  
244 3).

245  
246



247

248 **Figure 3. The change in the net top-of-atmosphere energy gain ( $R$ ) in the shortwave (a)**  
 249 **and in the longwave (b), and the change in the cloud radiative effect (CRE) in the**  
 250 **shortwave (c) and in the longwave (d), due to a change in the CO<sub>2</sub> concentration**  
 251 **(compared to the 1xCO<sub>2</sub> case of each aerosol concentration), for the different aerosol**  
 252 **concentrations (the different curves).**

253

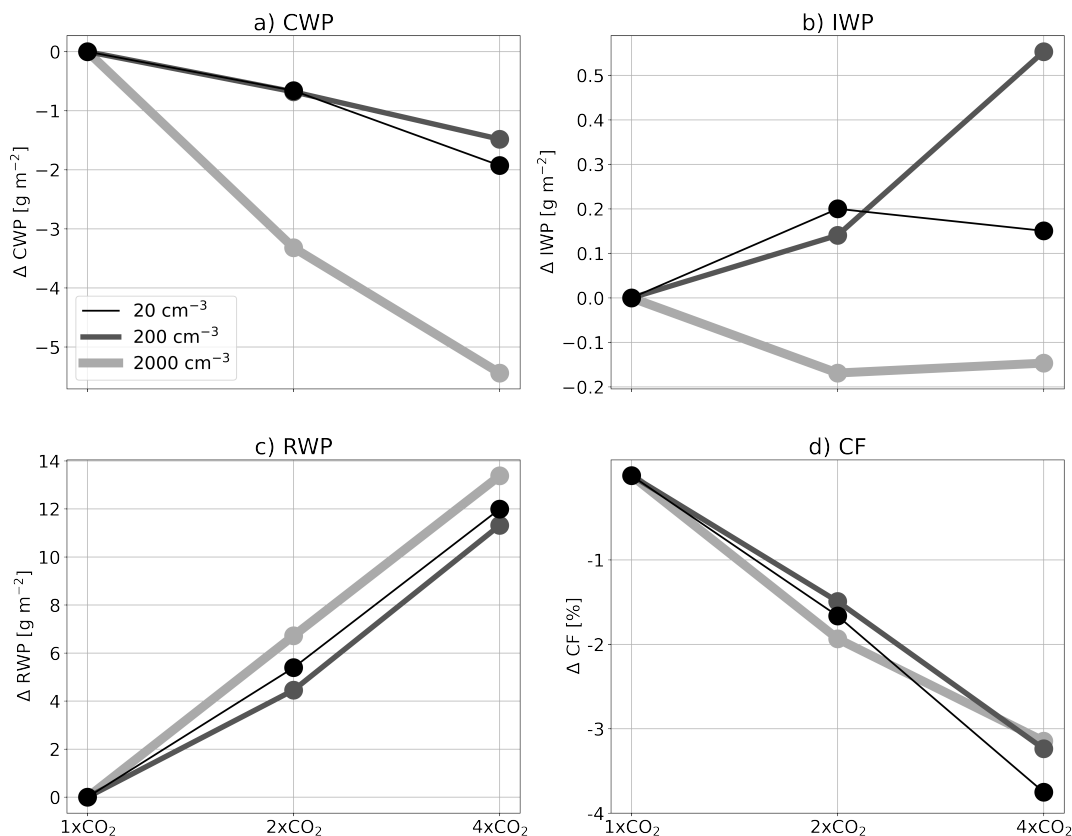
254 Thus far, we have seen that the ECS increases with  $N_a$  (Fig. 1 and Table 1) and that this  
 255 increase can be explained by changes in  $\lambda_{\text{cloud}}$  (Table 1) and specifically in  $CRE^{SW}$  (Fig.  
 256 3). To understand the changes in the cloud properties driving the changes in  $\lambda_{\text{cloud}}$ , and  
 257 hence also in ECS, under the different  $N_a$  conditions, in Fig. 4 we present the change in  
 258 cloud liquid water path (CWP), ice water path (IWP), rain water path (RWP) and cloud  
 259 fraction (CF) with increasing CO<sub>2</sub> concentrations for the different  $N_a$  conditions. The  
 260 figure shows that the CWP decreases with the CO<sub>2</sub> concentrations at a much faster rate  
 261 (about 3 times faster) under the highest  $N_a$  conditions compared to the low and medium  
 262  $N_a$  conditions (Fig. 4a). The changes in the IWP, on the other hand, are about an order  
 263 of magnitude smaller than the changes in CWP and are not consistent in sign for the  
 264 different  $N_a$  conditions (Fig. 4b). The RWP increases with the CO<sub>2</sub> concentrations at a  
 265 slightly faster rate (about 20% faster) under the highest  $N_a$  conditions compared to the

266 low and medium  $N_a$  conditions (however the response is non-monotonic with  $N_a$  - Fig.  
 267 4c). The CF decreases with the  $\text{CO}_2$  concentrations, at a similar rate for the different  $N_a$   
 268 conditions (about 1.5% decrease in CF for each doubling of the  $\text{CO}_2$  concentrations -  
 269 Fig. 4d).

270 The faster decrease in CWP with  $\text{CO}_2$  concentrations under high  $N_a$  conditions drives  
 271 the faster increase in  $\text{CRE}^{\text{SW}}$  as the clouds become less opaque in the shortwave. We  
 272 note that the difference in  $\text{CRE}^{\text{SW}}$  trend under different  $N_a$  conditions could not be  
 273 explained by the minor differences in the CF trends. In addition, the small differences  
 274 in the IWP between the different  $N_a$  conditions are consistent with the small differences  
 275 in the  $\text{CRE}^{\text{LW}}$  seen above. The general increase in RWP with  $\text{CO}_2$  concentrations is  
 276 consistent with an increase in rain efficiency with warming (Lutsko and Cronin, 2018),  
 277 as elaborated below.

278

279



280

281 **Figure 4. The change in: a) cloud liquid water path (CWP), b) ice water path (IWP), c)**  
 282 **rain water path (RWP), and d) cloud fraction (CF) due to a change in the  $\text{CO}_2$**   
 283 **concentration (compared to the 1x $\text{CO}_2$  case of each aerosol concentration), for the**  
 284 **different aerosol concentrations (the different curves).**

285 Figure 4 suggests that the largest difference in the cloud response to CO<sub>2</sub> under different  
286  $N_a$  conditions is due to changes in CWP. The higher sensitivity of CWP to CO<sub>2</sub>  
287 concentration under higher  $N_a$  conditions can explain the higher  $\lambda_{\text{cloud}}$  and thus also the  
288 larger ECS. Hence, the question arises: What causes the faster reduction in CWP with  
289 CO<sub>2</sub> concentration under high  $N_a$  conditions? A major sink for CWP is via precipitation.  
290 Hence, in Fig. 5 we present the change in the mean surface precipitation rate, the  
291 hydrological sensitivity ( $\eta$  - the rate of change in the surface precipitation per 1K  
292 increase in surface temperature) and the precipitation efficiency ( $\epsilon$ - calculated  
293 following Li et al. (2022) as the ratio of surface precipitation-to-condensed water path,  
294 i.e., CWP+IWP+RWP). Please note that the precipitation efficiency definition used  
295 here, following Li et al. (2022), is slightly different from the definition used in Lutsko  
296 and Cronin (2018). However, the two different definitions were shown to be tightly  
297 correlated (Li et al., 2022), thus, the exact definition used is not expected to change the  
298 main conclusions. In addition, the use of this definition will enable easier comparison  
299 with observations and global climate models in the future.

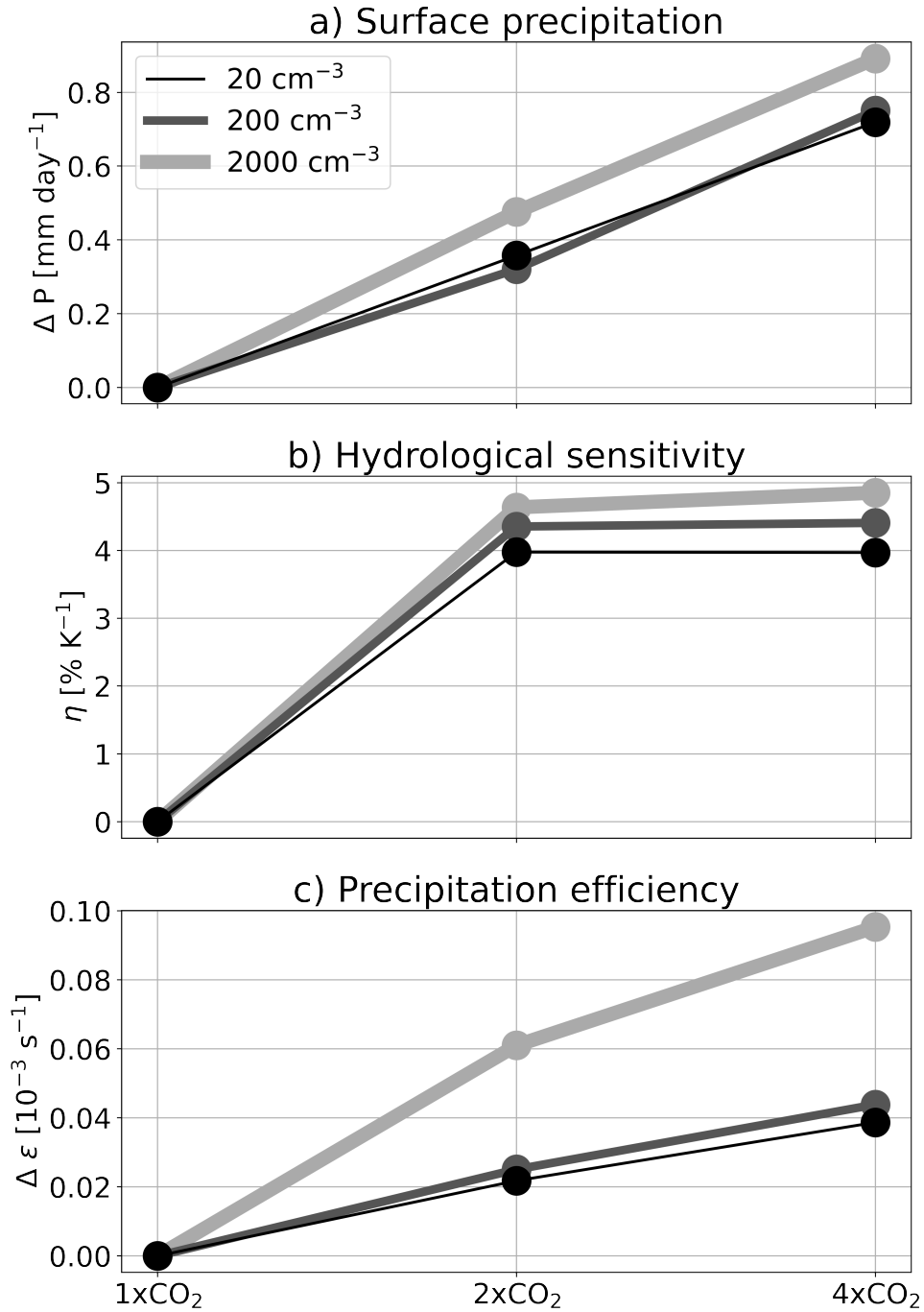
300 As expected, Fig. 5 demonstrates that the surface precipitation increases with CO<sub>2</sub> (i.e.,  
301  $\eta$  is positive) and so does  $\epsilon$  (Lutsko and Cronin, 2018). This is true for all  $N_a$  conditions.  
302 However, the rates of increase in surface precipitation and  $\epsilon$  with CO<sub>2</sub> concentration  
303 are higher under the highest  $N_a$  conditions (see also Table 1). We note that the larger  
304 rate of increase in surface precipitation under the highest  $N_a$  conditions is not solely due  
305 to the higher surface temperature increase, as  $\eta$  also increases with  $N_a$ .

306 The much larger (more than double- Table 1) rate of increase in  $\epsilon$  with the CO<sub>2</sub>  
307 concentration under the highest  $N_a$  conditions represents more efficient depletion of the  
308 cloud water from the atmosphere, leading to a faster reduction in CWP with CO<sub>2</sub>  
309 concentration (Fig. 4), which in turn leads to higher  $\lambda_{\text{cloud}}$  and ECS. The faster increase  
310 in RWP with CO<sub>2</sub> concentration under the highest  $N_a$  conditions presented in Fig. 4c is  
311 consistent with this explanation.

312

313

314



315

316 **Figure 5. The change in: a) surface precipitation, b) hydrological sensitivity ( $\eta$ ), and c)**  
 317 **precipitation efficiency ( $\epsilon$ ) due to a change in the CO<sub>2</sub> concentration (compared to the**  
 318 **1xCO<sub>2</sub> case of each aerosol concentration), for the different aerosol concentrations (the**  
 319 **different curves).**

320

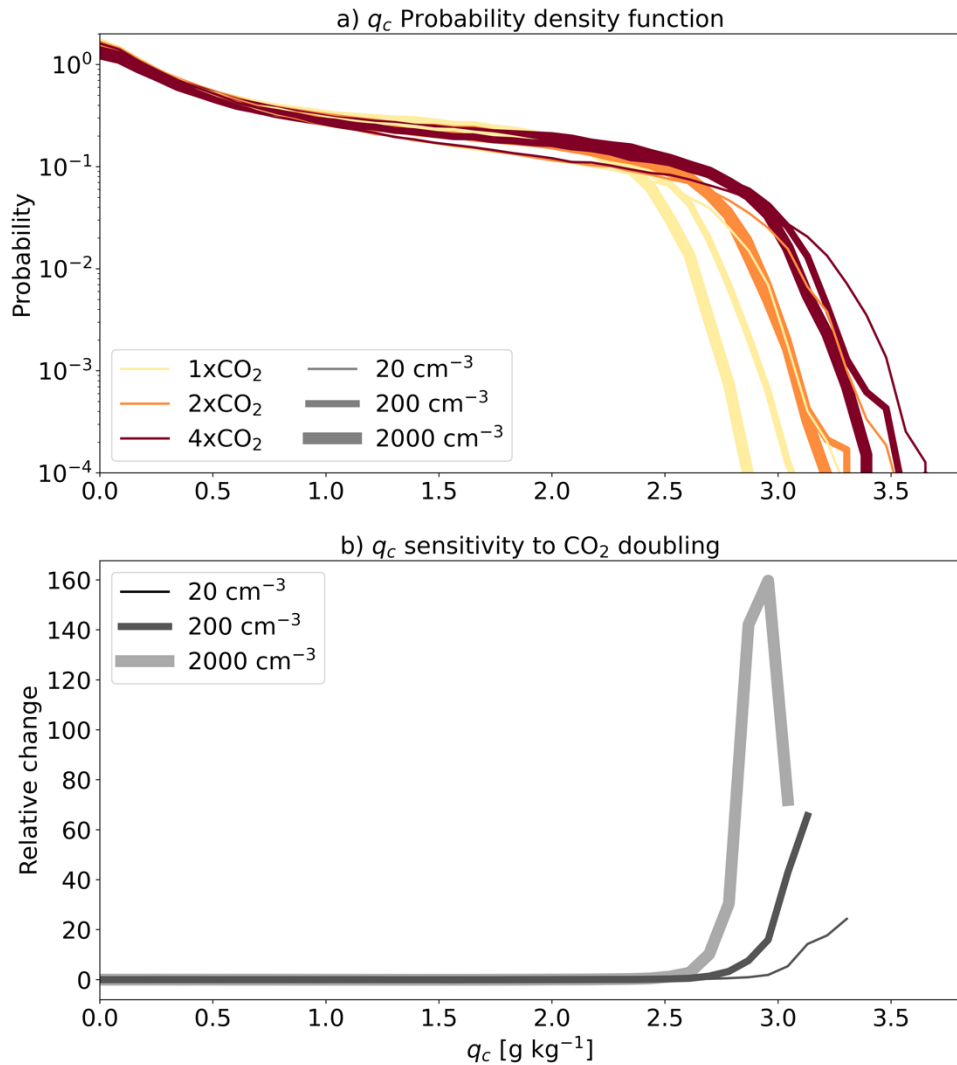
321 The last open question is why  $\epsilon$  increases faster with CO<sub>2</sub> concentration under the  
 322 highest  $N_a$  conditions. The increase in  $\epsilon$  with warming was shown to be mostly driven  
 323 by an increase in the efficiency with which cloud condensate is converted into

324 precipitation (Lutsko and Cronin, 2018). As was mentioned in the introduction, the  
325 conversion of cloud condensate into precipitation (or autoconversion of cloud droplets)  
326 becomes significant only when liquid water amount and/or droplet radii reach a critical  
327 threshold (Freud and Rosenfeld, 2012). To understand the faster  $\epsilon$  increases with CO<sub>2</sub>  
328 concentration under the highest  $N_a$  conditions, we present the histograms over the  
329 domain and time (during the last 150 days of the simulations based on 3D output in 1-  
330 hour resolution) of liquid cloud droplets mixing ratio ( $q_c$  – Fig. 6) and mean cloud  
331 droplet radii ( $\bar{r}_c$  – Fig. 7) around the height of the maximum in cloud droplet effective  
332 radii (1950m) and its mean sensitivity to doubling of CO<sub>2</sub> concentration for each  $N_a$   
333 condition.

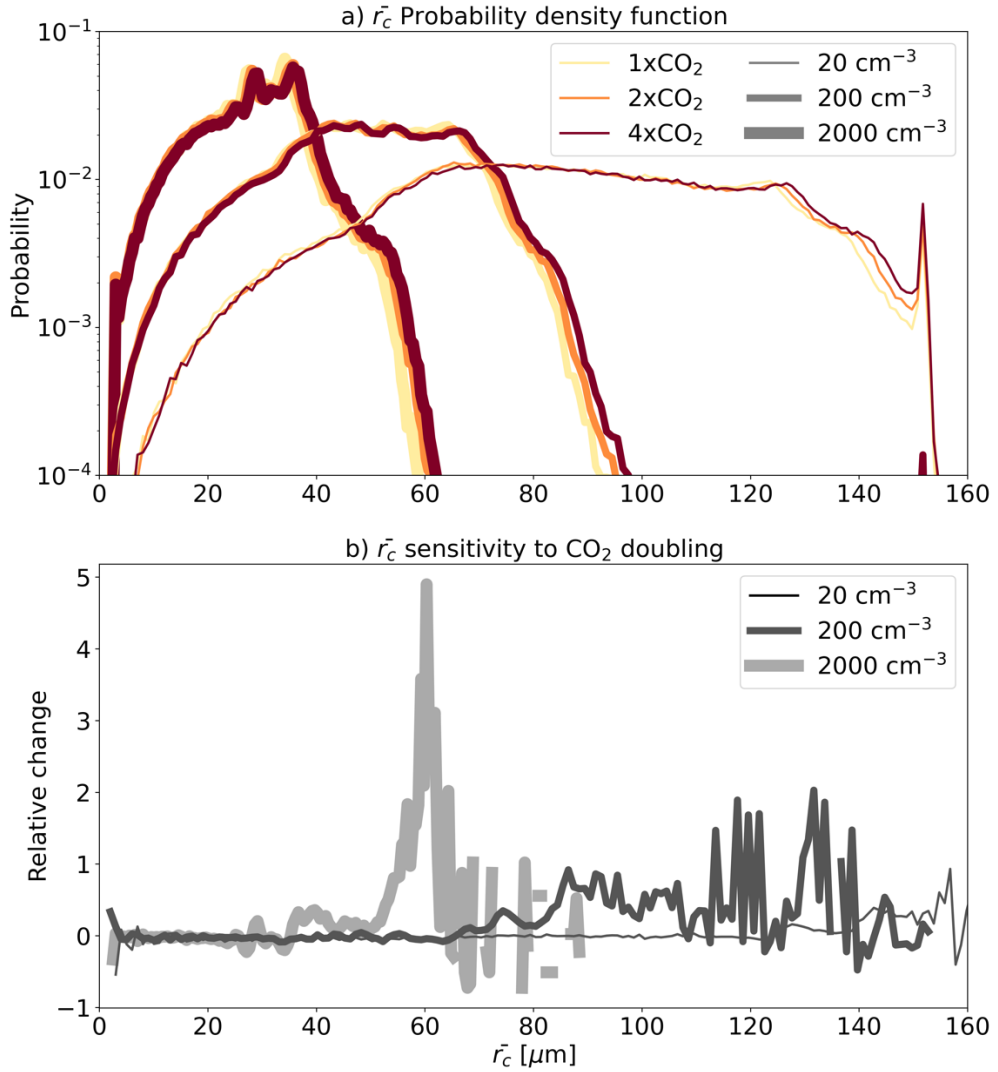
334 Figure 6 demonstrates that the cut-off of the  $q_c$  distribution (the mixing ratio for which  
335 the probability density function starts to decrease sharply) increases with the CO<sub>2</sub>  
336 concentration and decreases with the aerosol concentration. However, the sensitivity of  
337 the relatively large  $q_c$  with CO<sub>2</sub> concentration is significantly larger under high aerosol  
338 concentrations compared to the lower aerosol concentrations (Fig. 6b). The larger  
339 relative increase in high  $q_c$  promotes the autoconversion process and hence enhances  $\epsilon$ ,  
340 more under high aerosol concentrations than under low aerosol concentrations.

341 Figure 7 demonstrates, in line with expectations, that  $N_a$  has a strong effect on  $\bar{r}_c$ . In  
342 addition, it shows that under all  $N_a$  conditions,  $\bar{r}_c$  increases with the CO<sub>2</sub> concentration.  
343 This could be explained by the increase in the availability of water vapor (Fig. 2),  
344 which, for a given  $N_a$  conditions, enable larger diffusional growth of the droplets. This  
345 trend could also be understood from the increase in  $q_c$  with warming (Fig. 6, Lutsko  
346 and Cronin 2018), which under a given  $N_a$  conditions implies larger  $\bar{r}_c$ . Here again, the  
347 highest  $N_a$  conditions demonstrate the largest sensitivity of  $\bar{r}_c$  to CO<sub>2</sub> concentration,  
348 especially at the right-hand side of the distribution (Fig. 7b). This could be explained  
349 by the fact that under these high  $N_a$  conditions, the cloud droplet growth is primarily  
350 limited by the availability of water vapor, as large number of droplets compete for the  
351 available water vapor (Koren et al., 2014; Dagan et al., 2015a; Reutter et al., 2009).  
352 Thus, an increase in the availability of water vapor with CO<sub>2</sub> concentration (Fig. 2)  
353 under polluted conditions results in a larger increase in  $\bar{r}_c$  compared with clean  
354 conditions. However, the reasons behind this trend, as well as behind the larger increase  
355 in  $q_c$  in high- $N_a$  simulations deserve further exploration in the future. Similarly to the  
356  $q_c$  case, the larger relative increase in the relatively large droplets promotes the

357 autoconversion process and hence enhances  $\epsilon$ , more under high aerosol concentrations  
 358 than under lower aerosol concentrations.  
 359  
 360



361  
 362 **Figure 6. Probability density functions (PDF) of the cloud droplet mixing ratio ( $q_c$ ) for the**  
 363 **different simulations (a), and the mean sensitivity of the  $q_c$  PDF to a doubling of the CO<sub>2</sub>**  
 364 **concentration based on the three combinations available for each  $N_a$  condition [2xCO<sub>2</sub>-**  
 365 **1xCO<sub>2</sub>, 4xCO<sub>2</sub>-2xCO<sub>2</sub> and (4xCO<sub>2</sub>-1xCO<sub>2</sub>)/2] (b), calculated for the heights around which**  
 366 **the cloud droplet effective radii reach a maximum (1950m) and using 3-D files output**  
 367 **every hour of the last 150 days of the simulations. Note the logarithmic scales for the y-**  
 368 **axes of a.**  
 369



370

371 **Figure 7. Probability density functions (PDF) of cloud droplet mean radii ( $\bar{r}_c$ ) for the**  
 372 **different simulations (a), and the mean sensitivity of the  $\bar{r}_c$  PDF to a doubling of the CO<sub>2</sub>**  
 373 **concentration based on the three combinations available for each  $N_a$  condition [2xCO<sub>2</sub>-**  
 374 **1xCO<sub>2</sub>, 4xCO<sub>2</sub>-2xCO<sub>2</sub> and (4xCO<sub>2</sub>-1xCO<sub>2</sub>)/2] (b), calculated for the heights around which**  
 375 **the cloud droplet effective radii reach a maximum (1950m) and using 3-D files output**  
 376 **every hour of the last 150 days of the simulations. Note the logarithmic scales for the y-**  
 377 **axes of a.**

378

#### 379 4. Summary and conclusions

380 The role of clouds in a climate-change is manifested by two pathways: (1) effects of  
 381 anthropogenic aerosol on clouds, and (2) feedback that clouds exert on the changing  
 382 climate. These two pathways are usually studied separately, and even by different

383 scientific communities. In this paper, we demonstrate that the two pathways are closely  
384 linked to each other and should be examined concurrently.

385 Using long, idealized RCE simulations over a small domain with a slab ocean model,  
386 we demonstrate that the ECS, i.e., the increase in surface temperature under equilibrium  
387 conditions due to doubling of the CO<sub>2</sub> concentration, increases with the aerosol  
388 concentration. The ECS increase is explained by a faster increase in precipitation  
389 efficiency with warming under high aerosol concentrations, which represents a more  
390 efficient depletion of the water from the cloud and thus is manifested as an increase in  
391 the cloud feedback parameter. The precipitation efficiency increases faster under high  
392 aerosol concentration due to a higher sensitivity of the relatively high liquid water  
393 mixing ratios and the relatively large mean droplet sizes to a CO<sub>2</sub> concentration  
394 increase. We note that the increase in the total (shortwave plus longwave) cloud  
395 feedback parameter with the increase in precipitation efficiency is a result of a stronger  
396 shortwave effect (Li et al., 2019) than a longwave effect (Lindzen et al., 2001) in the  
397 simulations presented here. Future work should examine the robustness of this trend in  
398 different models, and with different microphysical and radiative schemes. Moreover,  
399 the response of precipitation to changes in aerosol concentration might be  
400 microphysical representation depended (White et al., 2017), and hence should be  
401 examined in the future under different microphysical schemes (conceivably in a multi-  
402 model intercomparison project focusing on aerosol effect on RCE simulations).

403 The results presented here are based on idealized simulations over a small domain.  
404 Under more realistic conditions, other processes, not included here, that could affect  
405 the precipitation efficiency and hence the general trend will be introduced. In particular,  
406 convective self-aggregation could be of interest as, while it is inhibited in the small  
407 domain used here, it was shown to affect precipitation efficiency (Lutsko et al., 2021)  
408 and to be affected by aerosols (Nishant et al., 2019). Other processes that should be  
409 accounted for in future research include the presence of large-scale circulation and  
410 direct aerosol radiative effects (Dagan et al., 2019; Dingley et al., 2021). In addition,  
411 the results presented here suggest that the sensitivity of ECS to aerosol loading might  
412 not be linear (Table 1). Hence, the dynamical aerosol range present at different  
413 geographical locations would affect the total ECS trend.

414 The results presented here suggest a possible connection between cloud feedback and  
415 aerosol-cloud interactions. The regulation of aerosol emissions is known to be more  
416 effective than the effort to reduce greenhouse gas emissions. This, together with the

417 short lifetime of aerosols in the atmosphere, has resulted in a reduction in the value of  
418 the global mean aerosol effective radiative forcing in recent years (Quaas et al., 2022).  
419 If the conclusions of this paper hold under higher levels of complexity (e.g., large-scale  
420 circulation, convective self-aggregation, etc.) this might mean that the reduction in  
421 global aerosol emissions could lead to a reduction in ECS, which could compensate, at  
422 least partially, for the reduction in the negative forcing induced by aerosols (Quaas et  
423 al., 2022; Bellouin et al., 2019), thus providing yet additional motivation for reducing  
424 aerosol emissions globally.

425

#### 426 **Code availability**

427 SAM is publicly available at: <http://rossby.msrc.sunysb.edu/~marat/SAM.html>

428

#### 429 **Data availability**

430 The data presented in this study is publicly available at:  
431 <https://doi.org/10.5281/zenodo.7306706>.

432

#### 433 **Author contributions**

434 GD carried out the simulations and analyses presented and prepared the article.

435

#### 436 **Competing interests**

437 The authors declare that they have no conflict of interest.

438

#### 439 **Financial support**

440 This research was supported by the Israeli Science Foundation Grant (1419/21).

441

#### 442 **5. References**

- 443 Abbott, T. H., & Cronin, T. W. (2021). Aerosol invigoration of atmospheric convection  
444 through increases in humidity. *science*, 371(6524), 83-85 .  
445 Albrecht, B. A.: Aerosols, cloud microphysics, and fractional cloudiness, *Science* (New  
446 York, NY), 245, 1227, 1989.  
447 Bellouin, N., Quaas, J., Gryspeerdt, E., Kinne, S., Stier, P., Watson-Parris, D., Boucher,  
448 O., Carslaw, K., Christensen, M., and Daniaou, A.-L.: Bounding aerosol radiative  
449 forcing of climate change, *Reviews of Geophysics*, 2019.  
450 Ceppi, P., Brient, F., Zelinka, M. D., and Hartmann, D. L.: Cloud feedback mechanisms  
451 and their representation in global climate models, *WIREs Climate Change*, 2017.  
452 Collins, W. D., Rasch, P. J., Boville, B. A., Hack, J. J., McCaa, J. R., Williamson, D.  
453 L., Briegleb, B. P., Bitz, C. M., Lin, S.-J., and Zhang, M.: The formulation and

454 atmospheric simulation of the Community Atmosphere Model version 3 (CAM3),  
455 Journal of Climate, 19, 2144-2161, 2006.

456 Dagan, G., Koren, I., and Altaratz, O.: Competition between core and periphery-based  
457 processes in warm convective clouds—from invigoration to suppression, Atmospheric  
458 Chemistry and Physics, 15, 2749-2760, 2015a.

459 Dagan, G., Koren, I., and Altaratz, O.: Aerosol effects on the timing of warm rain  
460 processes, Geophysical Research Letters, 42, 4590-4598, 10.1002/2015GL063839,  
461 2015b.

462 Dagan, G., Stier, P., and Watson-Parris, D.: Contrasting response of precipitation to  
463 aerosol perturbation in the tropics and extra-tropics explained by energy budget  
464 considerations, Geophysical Research Letters, 2019.

465 Dingley, B., Dagan, G., and Stier, P.: Forcing convection to aggregate using diabatic  
466 heating perturbations, Journal of Advances in Modeling Earth Systems, 13,  
467 e2021MS002579, 2021.

468 Freud, E., and Rosenfeld, D.: Linear relation between convective cloud drop number  
469 concentration and depth for rain initiation, Journal of Geophysical Research:  
470 Atmospheres (1984–2012), 117, 2012.

471 Gettelman, A., and Sherwood, S.: Processes Responsible for Cloud Feedback, Current  
472 Climate Change Reports, 2, 179-189, 2016.

473 Held, I. M., and Soden, B. J.: Robust responses of the hydrological cycle to global  
474 warming, Journal of Climate, 19, 5686-5699, 2006.

475 Igel, A. L., and van den Heever, S. C.: Invigoration or Enervation of Convective Clouds  
476 by Aerosols?, Geophysical Research Letters, 48, e2021GL093804, 2021.

477 Khain, A. P.: Notes on state-of-the-art investigations of aerosol effects on precipitation:  
478 a critical review, Environmental Research Letters, 4, 015004 (015020 pp.)-015004  
479 (015020 pp.), 10.1088/1748-9326/4/1/015004, 2009.

480 Khairoutdinov, M., and Yang, C.-E.: Cloud-resolving modelling of aerosol indirect  
481 effects in idealised radiative-convective equilibrium with interactive and fixed sea  
482 surface temperature, Atmospheric Chemistry and Physics, 13, 4133-4144, 2013.

483 Khairoutdinov, M. F., and Randall, D. A.: Cloud resolving modeling of the ARM  
484 summer 1997 IOP: Model formulation, results, uncertainties, and sensitivities, Journal  
485 of the Atmospheric Sciences, 60, 2003.

486 Koren, I., Kaufman, Y. J., Rosenfeld, D., Remer, L. A., & Rudich, Y. (2005). Aerosol  
487 invigoration and restructuring of Atlantic convective clouds. *Geophysical research  
488 letters*, 32(14) .(

489 Koren, I., Altaratz, O., Remer, L. A., Feingold, G., Martins, J. V., & Heiblum, R. H.  
490 (2012). Aerosol-induced intensification of rain from the tropics to the mid-latitudes.  
491 *Nature Geoscience* .

492 Koren, I., Dagan, G., and Altaratz, O.: From aerosol-limited to invigoration of warm  
493 convective clouds, science, 344, 1143-1146, 2014.

494 Li, R., Storelvmo, T., Fedorov, A. V., and Choi, Y.-S.: A positive IRIS feedback:  
495 Insights from climate simulations with temperature-sensitive cloud–rain conversion,  
496 Journal of climate, 32, 5305-5324, 2019.

497 Li, R. L., Studholme, J. H., Fedorov, A. V., and Storelvmo, T.: Precipitation efficiency  
498 constraint on climate change, Nature Climate Change, 12, 642-648, 2022.

499 Lindzen, R. S., Chou, M.-D., and Hou, A. Y.: Does the earth have an adaptive infrared  
500 iris?, Bulletin of the American Meteorological Society, 82, 417-432, 2001.

501 Loeb, N. G., Doelling, D. R., Wang, H., Su, W., Nguyen, C., Corbett, J. G., Liang, L.,  
502 Mitrescu, C., Rose, F. G., and Kato, S.: Clouds and the earth’s radiant energy system

503 (CERES) energy balanced and filled (EBAF) top-of-atmosphere (TOA) edition-4.0  
504 data product, *Journal of Climate*, 31, 895-918, 2018.

505 Lutsko, N., Sherwood, S. C., and Zhao, M.: Precipitation Efficiency and Climate  
506 Sensitivity (Invited Chapter for the AGU Geophysical Monograph Series " Clouds and  
507 Climate"), 2021.

508 Lutsko, N. J., and Cronin, T. W.: Increase in precipitation efficiency with surface  
509 warming in radiative-convective equilibrium, *Journal of Advances in Modeling Earth  
510 Systems*, 10, 2992-3010, 2018.

511 Mauritsen, T., and Stevens, B.: Missing iris effect as a possible cause of muted  
512 hydrological change and high climate sensitivity in models, *Nature Geoscience*, 8, 346,  
513 2015.

514 Morrison, H., Curry, J., and Khvorostyanov, V.: A new double-moment microphysics  
515 parameterization for application in cloud and climate models. Part I: Description,  
516 *Journal of the atmospheric sciences*, 62, 1665-1677, 2005.

517 Muller, C. J., and Held, I. M.: Detailed investigation of the self-aggregation of  
518 convection in cloud-resolving simulations, *Journal of the Atmospheric Sciences*, 69,  
519 2551-2565, 2012.

520 Mülmenstädt, J., and Feingold, G.: The Radiative Forcing of Aerosol–Cloud  
521 Interactions in Liquid Clouds: Wrestling and Embracing Uncertainty, *Current Climate  
522 Change Reports*, 4, 23-40, 2018.

523 Nishant, N., Sherwood, S. C., and Geoffroy, O.: Aerosol-induced modification of  
524 organised convection and top-of-atmosphere radiation, *npj Climate and Atmospheric  
525 Science*, 2, 1-10, 2019.

526 Nuijens, L., and Siebesma, A. P.: Boundary Layer Clouds and Convection over  
527 Subtropical Oceans in our Current and in a Warmer Climate, *Current Climate Change  
528 Reports*, 1-15, 2019.

529 Quaas, J., Jia, H., Smith, C., Albright, A. L., Aas, W., Bellouin, N., Boucher, O.,  
530 Doutriaux-Boucher, M., Forster, P. M., and Grosvenor, D.: Robust evidence for  
531 reversal in the aerosol effective climate forcing trend, *Atmospheric Chemistry and  
532 Physics Discussions*, 1-25, 2022.

533 Reutter, P., Su, H., Trentmann, J., Simmel, M., Rose, D., Gunthe, S., Wernli, H.,  
534 Andreae, M., and Pöschl, U.: Aerosol-and updraft-limited regimes of cloud droplet  
535 formation: influence of particle number, size and hygroscopicity on the activation of  
536 cloud condensation nuclei (CCN), *Atmospheric Chemistry and Physics*, 9, 7067-7080,  
537 2009.

538 Romps, D. M.: Climate sensitivity and the direct effect of carbon dioxide in a limited-  
539 area cloud-resolving model, *Journal of Climate*, 33, 3413-3429, 2020.

540 Rosenfeld, D.: Suppression of rain and snow by urban and industrial air pollution,  
541 *Science*, 287, 1793-1796, 10.1126/science.287.5459.1793, 2000.

542 Rosenfeld, D., Lohmann, U., Raga, G. B., O'Dowd, C. D., Kulmala, M., Fuzzi, S., et  
543 al. (2008). Flood or drought: How do aerosols affect precipitation? *science*, 321(5894),  
544 1309-1313. <Go to ISI>://WOS:000258914300038

545 Schneider, T., Teixeira, J., Bretherton, C. S., Brient, F., Pressel, K. G., Schär, C., and  
546 Siebesma, A. P.: Climate goals and computing the future of clouds, *Nature Climate  
547 Change*, 7, 3-5, 2017.

548 Sherwood, S., Webb, M. J., Annan, J. D., Armour, K., Forster, P. M., Hargreaves, J. C.,  
549 Hegerl, G., Klein, S. A., Marvel, K. D., and Rohling, E. J.: An assessment of Earth's  
550 climate sensitivity using multiple lines of evidence, *Reviews of Geophysics*, 58,  
551 e2019RG000678, 2020.

552 Twomey, S.: The nuclei of natural cloud formation part II: The supersaturation in  
553 natural clouds and the variation of cloud droplet concentration, *Geofisica pura e*  
554 *applicata*, 43, 243-249, 1959.

555 Twomey, S.: Pollution and the planetary albedo, *Atmospheric Environment* (1967), 8,  
556 1251-1256, 1974.

557 Twomey, S.: The influence of pollution on the shortwave albedo of clouds, *Journal of*  
558 *the atmospheric sciences*, 34, 1149-1152, 1977.

559 Warner, J., and Twomey, S.: The production of cloud nuclei by cane fires and the effect  
560 on cloud droplet concentration, *Journal of the atmospheric Sciences*, 24, 704-706, 1967.

561 White, B., Gryspeerdt, E., Stier, P., Morrison, H., Thompson, G., & Kipling, Z. (2017).  
562 Uncertainty from choice of microphysics scheme in convection-permitting models  
563 significantly exceeds aerosol effects. *Atmospheric Chemistry and Physics*, 7 .

564 Wing, A. A., Reed, K. A., Satoh, M., Stevens, B., Bony, S., and Ohno, T.: Radiative-  
565 convective equilibrium model intercomparison project, *Geoscientific Model*  
566 *Development*, 793-813, 2018.

567 Yanase, T., Nishizawa, S., Miura, H., Takemi, T., and Tomita, H.: New critical length  
568 for the onset of self-aggregation of moist convection, *Geophysical Research Letters*,  
569 47, e2020GL088763, 2020.

570

571

572

573